ROYAL SOCIETY
OF CHEMISTRY

PAPER

Check for updates

A highly sensitive electrochemical sensor for the detection of lead(ii) ions utilizing rice-shaped bimetallic MOFs incorporated reduced graphene oxide†

Tien Dat Doan,[ab] Thi Hai Yen Pham,[a] Dinh Dung Luong, [ID][a] Nhung Hac Thi,[ab] Ho Thi Oanh,[a] Thu Thao Le,[c] Ha Tran Nguyen, [ID][d] Thi Kim Dung Hoang [ID][e] and Mai Ha Hoang [ID] *[ab]

The detection of lead ions (Pb^{2+}) in water is of critical importance due to the harmful effects of lead on human health and the environment. Traditional detection methods often require high user expertise, expensive equipment, and complex analytical procedures. Electrochemical sensors have emerged as effective alternatives due to their portability and affordability. In this study, a novel electrochemical sensor was developed for the sensitive and selective detection of Pb^{2+} based on glassy carbon electrodes (GCE) modified with bimetallic metal–organic frameworks (MOFs) and reduced graphene oxide (rGO). The bimetallic MOFs were successfully synthesized *via* a hydrothermal method, combining two metal centers Fe and Mg linked to a 1,4-benzene dicarboxylate ligand (FeMg-BDC). The synthesized FeMg-BDC has higher conductivity and surface area than monometallic Fe-BDC or Mg-BDC MOFs. Thanks to the synergistic effects between FeMg-BDC and rGO, the rGO/FeMg-BDC electrode has a larger electrochemically active surface area and faster electron transfer rate than the bare GCE. This enhancement facilitated the accumulation of lead onto the electrode surface, thereby improving the sensitivity of Pb^{2+} ion detection. Using the square wave anodic stripping voltammetry method, the sensor based on rGO/FeMg-BDC electrode exhibited two linear ranges: 0.01 to 0.5 µg L^{-1} and 0.5 to 50.0 µg L^{-1}, with a low limit of detection (LOD) of 9 ng L^{-1}. Furthermore, the external rGO thin film protects the FeMg-BDC material on the electrode surface, ensuring high durability and repeatability of the sensor. The developed sensor was successfully applied to accurately determine lead ion concentrations in various real water samples.

1. Introduction

Nowadays, with the growth of metallurgy and chemical industries, significant quantities of heavy metal ions (HMIs) are released into aquatic ecosystems. The pollution caused by HMIs raises critical concerns due to their effect on environmental safety and human health.[1,2] Lead is known to be an extremely toxic

[a]*Institute of Chemistry, Vietnam Academy of Science and Technology, 18 Hoang Quoc Viet, Cau Giay, Hanoi 10072, Vietnam. E-mail: hoangmaiha@ich.vast.vn*

[b]*Graduate University of Science and Technology, Vietnam Academy of Science and Technology, 18 Hoang Quoc Viet, Cau Giay, Hanoi 10072, Vietnam*

[c]*Faculty of Chemistry, Hanoi National University of Education, 136 Xuan Thuy, Cau Giay, Hanoi 10072, Vietnam*

[d]*National Key Laboratory of Polymer and Composite Materials, Ho Chi Minh City University of Technology, Vietnam National University, Ho Chi Minh City 70000, Vietnam*

[e]*Institute of Chemical Technology, Vietnam Academy of Science and Technology, 1A Thanh Loc 29 Str., Dist. 12, Ho Chi Minh City 70000, Vietnam*

† Electronic supplementary information (ESI) available. See DOI: https://doi.org/10.1039/d4ra08952a

heavy metal, lead exposure poses a significant threat to human health across all ages, causing developmental problems in children, cardiovascular issues in adults, and a range of other health complications.[1,3,4] Human exposure to lead ions primarily arises from the ingestion of food or water that has been contaminated with lead. The World Health Organization (WHO) has established a maximum permissible limit of 10 µg L^{-1} for Pb^{2+} in drinking water.[5] Detection and determination of Pb^{2+} ions are an important research topic. The determination of metal ions is commonly performed using a variety of popular techniques such as flame atomic absorption spectroscopy (FAAS), inductively coupled plasma atomic emission spectrometry (ICP-AES), inductively coupled plasma mass spectrometry (ICP-MS), and atomic fluorescence spectroscopy (AFS).[6–9] However, although these methods provide high sensitivity and selectivity, they require high user expertise, expensive equipment, and complex analytical procedures.[10] Recently, electrochemical sensors have become contemporary recognition methods for chemical analysis due to their benefits of portability, and reasonable cost.[11,12] Lead or most

heavy metals possess their distinctive electrochemical reduction–oxidation activity, rendering them effortless and expedient to be directly recognized by taking advantage of their redox characteristics. Square wave anodic stripping voltammetry (SWASV) stands out as an electrochemical analysis technique offering exceptional sensitivity and low limits of detection (LOD). However, the performance of SWASV critically depends on the characteristics of the working electrode.[13–15] Hence, the selection of suitable materials to fabricate or modify working electrode plays an important role in improving the performance of electrochemical sensors. Metal–organic frameworks (MOFs) are porous, crystalline materials formed by linking metal ions with organic ligands.[16] MOFs are ideal materials for designing high-performance electrochemical sensors due to their high surface area, tunable porosity, potential for redox activity, and ability to incorporate functional groups.[17–20] However, a common limitation of monometallic metal–organic frameworks is relatively low electrical conductivity.[21–23] This drawback reduces charge transfer on the electrode surface.[19,20,24] To solve this issue, bimetallic MOFs were utilized to prepare the working electrode. By incorporating two different metal ions in their inorganic nodes, bimetallic MOFs synergistically enhance conductivity, facilitating efficient charge transfer within the framework.[25] For instance, Wang's group demonstrated that carbon cloth modified with a Ni/Co bimetal MOF displayed remarkable electron transport properties and catalytic performance for glucose sensing.[21] In addition to enhancing electron conductivity, prior studies have demonstrated that FeMg-BDC MOFs exhibit remarkable heavy metal ion adsorption capabilities.[26,27] Consequently, the bimetallic FeMg-BDC is also expected to promote the adsorption of lead ions onto the electrode surface during the accumulation process. As a result, electrochemical sensors incorporating FeMg-BDC material hold great potential for achieving exceptional sensitivity in Pb^{2+} analysis.

Building on this, our study presents the initial application of the bimetallic MOF FeMg-BDC as an electrode material for a trace-level Pb^{2+} electrochemical sensor. Despite its promising sensitivity, the weak adhesion between the FeMg-BDC layer and the electrode surface was found to diminish the durability of the sensor. To address this limitation, a reduced graphene oxide (rGO) coating was introduced to improve the stability and performance of the electrode. Although previous studies have explored MOF-graphene hybrids for electrochemical sensing, the specific role of rGO in enhancing electrode durability and charge transfer has not been well elucidated.[20,28] This work demonstrates that the rGO/FeMg-BDC/GCE electrode achieves superior sensitivity for Pb^{2+} detection and significantly improves durability compared to the unmodified FeMg-BDC/GCE. Additionally, the rGO/FeMg-BDC/GCE sensor accurately detected Pb^{2+} concentrations in various real water samples, underscoring its potential for practical applications in continuous monitoring.

2. Experimental

2.1. Materials

Graphite powder (size less than 20 μm), standard solution of Pb^{2+} (1000 mg L^{-1}), terephthalic acid (H_2BDC) (98%),

$FeCl_3 \cdot 6H_2O$ (99%), $Mg(NO_3)_2 \cdot 6H_2O$ (98%), $K_3[Fe(CN)_6]$ (99%), $K_4[Fe(CN)_6] \cdot 3H_2O$ (98%), KOH (90%), KH_2PO_4 (99.5%), K_2HPO_4 (98%), H_3PO_4 (85%), CH_3COOH (99%), CH_3COONa (99%), KCl (99.5%), $NaNO_3$ (99%), $KMnO_4$ (98%), H_2SO_4 (98%), dimethylformamide (DMF) were obtained from Sigma Aldrich. Deionized (DI) water and ethanol (C_2H_5OH) were used for solution preparation, cleaning, and other purposes.

2.2. Apparatus

The morphology of materials and electrodes was characterized by field emission scanning electron microscopy (FESEM, JSM-IT800/JEOL, Japan) and high-resolution transmission electron microscopy (TEM, JEM 1400, JEOL, Japan). X-ray photoelectron spectroscopy (XPS, Thermo VG, Multilab 2000, England) was carried out to study the chemical states and the elemental composition of the samples. The crystal structures were confirmed by X-ray diffractometer (XRD, Bruker D8 Advance). Specific surface areas of MOF materials were investigated by Brunauer–Emmett–Teller (BET) method (Tristar-3030 system, USA Micromeritics). The presence of functional groups in the material was determined by Fourier-transform infrared (FT-IR) spectroscopy (Jacos 4700 spectrometer, USA) and Raman spectroscopy (LabRAM HR Evolution, Horiba, France). The zeta potential of bimetallic MOF and graphene oxide dispersed in water was determined using dynamic light scattering with a Litesizer 500 instrument (Anton Paar, Austria).

Electrochemical measurements utilized an AUTOLAB PGS302N device (Metrohm, Netherland) with a three-electrode system: a reference electrode (Ag/AgCl/KCl), a counter electrode (platinum wire), and a developed working electrode. Techniques included electrochemical impedance spectroscopy (EIS), cyclic voltammetry (CV), and square wave anodic stripping voltammetry (SWASV) were used for the examination of the electrochemical properties of the electrodes and Pb^{2+} analysis procedures.

2.3. Synthesis of GO

GO was synthesized by the modified Hummers' method by oxidizing graphite with HNO_3, H_2SO_4, and $KMnO_4$.[29] The synthesis process was carried out as follows: 1 g of graphite was dispersed in 50 mL of a concentrated H_2SO_4/HNO_3 solution (the ratio of the two acids was 3 : 1). The mixture was maintained at 0 °C, and 1 g of $KMnO_4$ was gradually added, followed by stirring for 20 hours. After the reaction, the solid was filtered and washed with distilled water multiple times to eliminate residual acid thoroughly. After synthesis, the GO was obtained in gel form at a concentration of 1 mg mL^{-1}.

2.4. Synthesis of MOFs

Bimetallic FeMg-BDC frameworks were prepared according to the previous literature[27] with some modifications, specifically as follows: A series of FeMg-BDC materials were synthesized with varying Fe/Mg ratios. Briefly, 1 mmol of a mixture of metal salts ($FeCl_3 \cdot 6H_2O$ and $Mg(NO_3)_2 \cdot 6H_2O$) with desired molar ratios of Fe^{3+}/Mg^{2+} (1/1, 1/2, 1/4) was mixed with 1 mmol of H_2BDC in 10 mL of DMF. The mixture was continuously stirred until

a homogeneous solution was formed. Then, 2 mL of 0.2 M NaOH solution was added to the mixture, and stirring continued for 15 min. The mixture was then transferred to an oven at 100 °C for 12 hours. The resulting mixture was then cooled to room temperature. After that, the synthesized MOFs were washed by centrifugation several times with DMF and ethanol to remove unreacted substances before drying at 80 °C for 24 h under vacuum. The obtained powder was denoted as FeMg-BDC (1/1), FeMg-BDC (1/2), and FeMg-BDC (1/4), corresponding to the Fe/Mg ratio. For comparison, monometallic Fe-BDC and Mg-BDC were also prepared using the same procedure.

2.5. Modification of the glassy carbon electrode

The GCE surface was first polished with sandpaper, then, it was cleaned with ethanol and dried. The 1 mg mL^{-1} MOF solution was prepared by dispersing the MOF uniformly in DI water via ultrasonication for 15 minutes. After that, 4 µL of MOF solution was drop-coated onto the surface of the GCE, followed by drying with infrared lights for 15 minutes. The resulting MOF electrodes were labeled as Fe-BDC, Mg-BDC, and FeMg-BDC electrodes.

Then, GO was drop-coated onto the FeMg-BDC electrode surface to form the GO/FeMg-BDC electrode. The GO/FeMg-BDC electrodes were electrochemically reduced by cyclic voltammetry within the potential range from 0 to −1 V in a 0.1 M PBS solution at pH 7 for a total of 10 cycles to obtain rGO/FeMg-BDC electrode.[30]

2.6. Pb^{2+} analysis

Pb^{2+} was analyzed by SWASV in KCl–HCl solution. The modified electrode was immersed in a Pb^{2+} solution at a deposition potential of −0.8 V before being scanned from −0.8 V to 0 V to record the oxidation signals of Pb. Electrode materials, deposition potential, pH of the electrolyte solution, and deposition potential, accumulation time were investigated to optimize before developing the linear ranges curve.

3. Result and discussion

3.1. Characterization of synthesized MOFs

FESEM images show that the Fe-BDC crystal had a rice-shaped morphology with a typical length ranging from 800 to 1000 nm and an average diameter of approximately 100 nm (Fig. 1a). Meanwhile, the obtained Mg-MOFs exhibit undefined morphology and irregular dimensions (Fig. 1e). The bimetallic FeMg-BDC frameworks maintain a similar morphology with Fe-BDC (Fig. 1b–d). However, the incorporation of Mg into the FeMg-BDC framework results in a slight change in crystal size. Specifically, as the Mg content in the MOF increases, the length of the bimetallic FeMg-BDC (n) crystals gradually decreases. Besides, the FESEM of FeMg-BDC (1/4) reveals the presence of rice-shaped crystals of the bimetal MOF alongside crystals resembling the Mg-BDC morphology. The resulting product emerges as a composite, comprising both the bimetal MOF and the monometallic Mg-BDC.

The presence of metals in bimetallic-MOF crystals was investigated by EDS spectroscopy. The EDS spectrum in
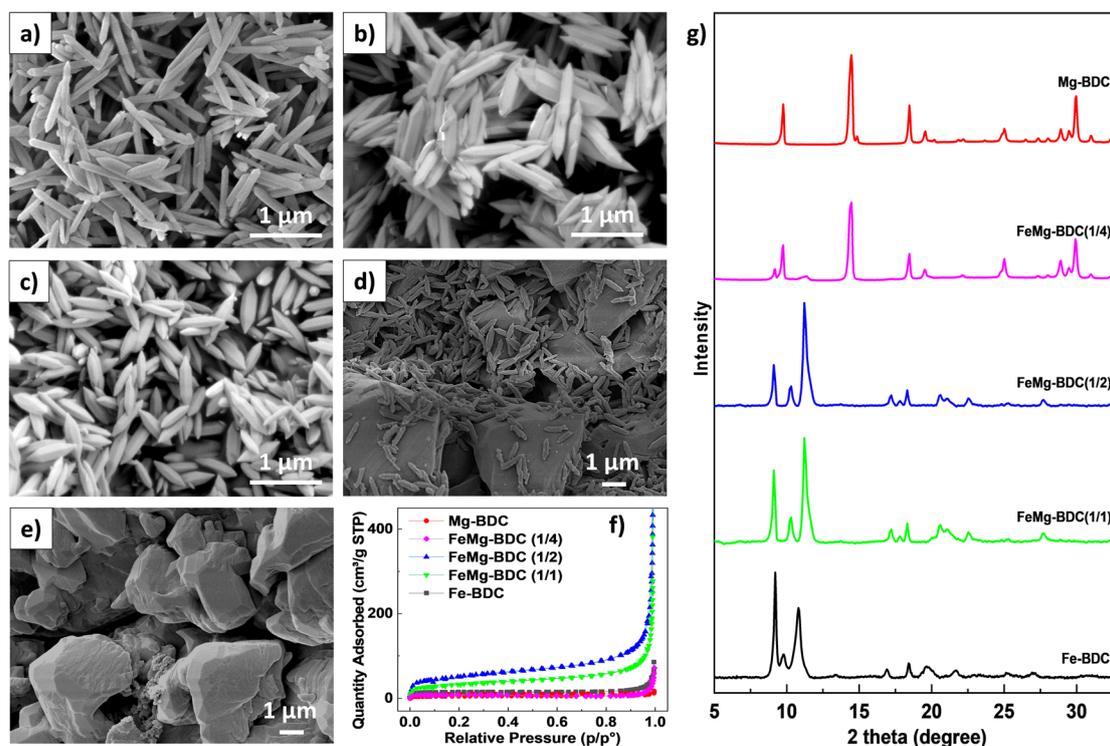

Fig. 1 SEM images of MOFs: (a) Fe-BDC, (b) FeMg-BDC (1/1), (c) FeMg-BDC (1/2), (d) FeMg-BDC (1/4), (e) Mg-BDC, (f) N$_2$ adsorption–desorption isotherms and (g) XRD patterns of MOF samples.

Fig. S1a† confirms the presence of both Fe and Mg in the bimetallic MOF. Moreover, the FESEM elemental mapping images in Fig. S1b† reveal a uniform distribution of Fe, and Mg confirming the coexistence of both Fe and Mg metal within the bimetal FeMg-BDC crystal.

The crystallization behaviors of the synthesized MOFs were determined by XRD patterns. In Fig. 1g, the sharp and prominent peaks indicate that the synthesized MOF materials are all highly crystalline. The XRD pattern of the synthesized Fe-BDC sample exhibits distinct diffraction peaks at $2\theta \sim 9°$ and $11°$ corresponding to the (100) and (101) planes, respectively. For the synthesized Mg-BDC, the XRD pattern shows diffraction peaks at $2\theta \sim 9.5°$, $14.4°$, $18.6°$, $24°$ and $28.5°$. Compared with the simulated pattern,[31] and the previously reported results,[26,27] it can be seen that Fe-BDC and Mg-BDC were successfully synthesized. The XRD patterns of the bimetallic FeMg-BDC (1/1 and 1/2) reveal that with reducing Fe/Mg ratio, the intensity of the diffraction peak at about 9° increases, while the intensity of the diffraction peak around 11° decreases. This phenomenon indicates the successful incorporation of Mg into the framework, consistent with prior reports on Fe and Mg bimetallic MOFs.[26,27] Meanwhile, the XRD pattern of FeMg-BDC (1/4) exhibits strong intensity peaks of Mg-BDC and some weak intensity peaks of bimetallic FeMg-BDC. Therefore, the main crystalline phase of FeMg-BDC (1/4) is Mg-BDC and the rest is bimetallic FeMg-BDC. This result is consistent with the FESEM image in Fig. 1d.

The chemical state of elements in the FeMg-BDC was also determined *via* X-ray photoelectron spectroscopy (XPS). The overall survey spectra in Fig. 2a reveal the presence of Fe, Mg, C, and O. The Mg 1s peak at 1304.2 eV confirms the incorporation of Mg into the bimetallic MOF (Fig. 2b). The Fe 2p spectrum of the FeMg-BDC (Fig. 2c) is deconvoluted into two characteristic peaks of the Fe $2p_{3/2}$ peak at 711.4 and the Fe $2p_{1/2}$ peak at 725.08 eV. Additionally, the Fe 2p spectrum also indicates the presence of Fe^{2+} (711.15, 724.77 eV) and Fe^{3+} (712.85, 727.43 eV) with satellite peaks (717.85, 731.26 eV), suggesting the presence of Fe in both oxidation states within the structure of the FeMg-BDC molecule. The O 1s spectra have two distinct peaks at 531.48 and 532.14 eV, which correspond to the carboxyl groups of the BDC linker and the Fe/Mg–O bonds of FeMg-BDC, respectively (Fig. 2d).[27]

In addition, the specific surface areas and porosity of the synthesized MOF are also investigated through nitrogen adsorption/desorption analyses. As shown in Fig. 1f and Table 1, the BET surface areas of the as-synthesized Fe-BDC and Mg-BDC are 47.53 and 17.26 m^2 g^{-1}, respectively. Notably, the combination of Fe and Mg in the MOF structure significantly increased the BET surface area of the bimetallic MOF, reaching a maximum value of 182.24 m^2 g^{-1} at the Fe/Mg ratio of 1/2. The pore volume and pore size of this MOF are also the largest, measuring 1.36 cm^3 g^{-1} and 16.44 nm, respectively. This increase is attributed to the synergistic effect between Fe and Mg, as well as the high dispersion of Fe crystals within the porous structure of Mg-MOF. The lower BET surface area observed at the Fe/Mg ratio of 1/1 (129.02 m^2 g^{-1}) is likely due to the aggregation of Fe species in the structure.[26] Conversely, when the Mg content increases significantly with the Fe/Mg ratio of 1/4, the Mg-BDC phase predominates, as clearly observed in the SEM and XRD images, resulting in a lower BET
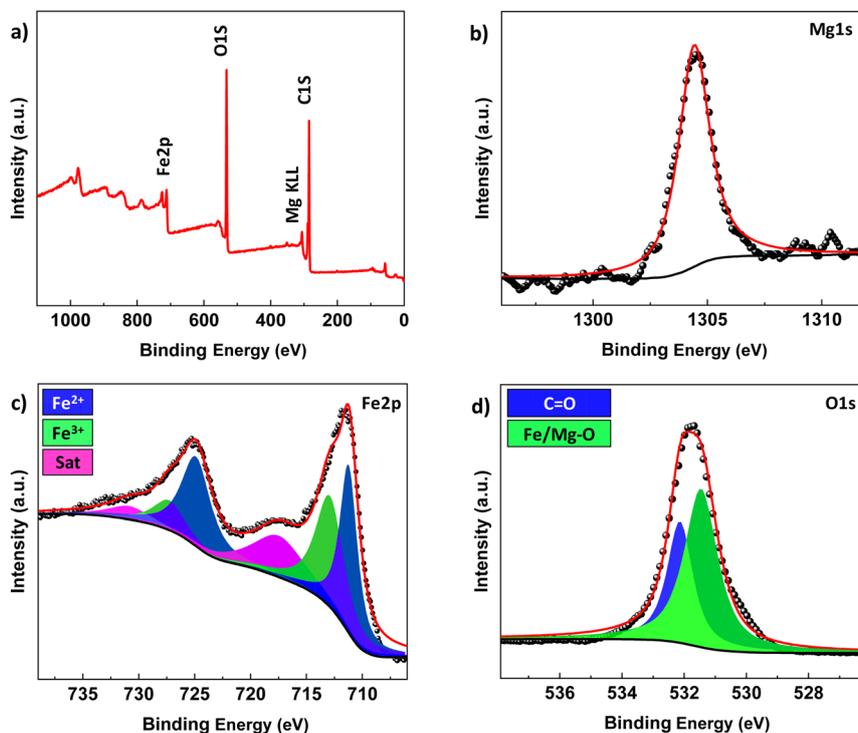

Fig. 2 XPS spectra of the bimetallic Fe−Mg−BDC: (a) overall survey spectrum, (b) Mg 1s, (c) Fe 2p, (d) O 1s.

Table 1 BET surface area, pore volume, and pore size of MOF materials

Material	BET surface area m^2 g^{-1}	Pore volume cm^3 g^{-1}	Pore size nm
Fe-BDC	47.53	0.09	3.39
Fe–Mg-BDC (1/1)	129.02	0.55	5.45
Fe–Mg-BDC (1/2)	182.24	1.36	16.44
Fe–Mg-BDC (1/4)	22.37	0.08	4.31
Mg-BDC	17.26	0.02	2.39

surface area of Fe–Mg-BDC (1/4) of only 22.37 m^2 g^{-1}. This trend is consistent with previous studies by W. S. Abo El-Yazeed and Y. Gu.[26,27]

The zeta potential of the synthesized bimetallic MOF was investigated, as depicted in Fig. S1c.† The measured zeta potential for the bimetallic MOF sample is approximately −10.8 mV indicates that the surface of the MOF carries a negative charge. This charge originates from carboxylate functional groups (–COO$^-$) on the MOF surface, which dissociate in the aqueous environment, leaving behind negatively charged sites. These sites facilitate the adsorption of Pb^{2+} cations in the aqueous phase through electrostatic attraction.[32,33]

3.2. Properties of modified electrodes

The surface morphology of FeMg-BDC, GO/FeMg-BDC, and rGO/FeMg-BDC electrodes were observed by field emission scanning electron microscopy (Fig. 3). The MOF crystal is uniformly distributed on the surface of the GCE electrodes. Fig. 3c and d reveals the presence of a graphene oxide (GO) layer on the surface of the MOF material. After the electrochemical reduction process, the rGO/FeMg-BDC electrode surface is still similar to the GO/FeMg-BDC electrode and the morphology of FeMg-BDC MOF crystals remains unchanged (Fig. 3e and f), indicating that the electrochemical reduction did not affect the bimetallic MOF material layer. The incorporation of the GO or rGO layer is expected to enhance the durability of the electrode.

Electrochemical characterization of the prepared electrodes was analyzed by electrochemical impedance spectra (EIS) and cyclic voltammograms (CV).

EIS results are shown in Fig. 4a and b and the equivalent circuit is displayed in the inset. Based on EIS analysis, the GCE has a total electrode impedance (R_{ct}) value of 180 Ω. After modification with monometallic MOF, the R_{ct} values of the Fe-BDC and Mg-BDC electrodes increase to 229 Ω and 398 Ω, respectively. This result shows that the monometallic MOF reduces the charge transfer ability on the electrode surface due to its low conductivity. In contrast, the FeMg-BDC electrode has a significantly lower R_{ct} than the GCE (∼70 Ω), which shows that bimetallic MOF material can accelerate the charge transfer on the modified electrode surface. The R_{ct} value of the GO/FeMg-BDC electrode is 413 Ω, which is higher than that of the FeMg-BDC electrode. This can be explained by the poor conductivity of GO, which disrupts electron transfer and leads to reduced conductivity. Meanwhile, due to the high electrical conductivity of rGO, the R_{ct} value of the rGO/FeMg-BDC electrode is the lowest, at just 55.7 Ω.

CV results are indicated in Fig. 4c, the Fe-BDC and Mg-BDC electrodes show lower redox peak current values (I_p), and peak-to-peak separation (ΔE_p) is wider than GCE. This phenomenon is explained by the low electrical conductivity of monometallic MOFs. Meanwhile, the FeMg-BDC electrode has a lower ΔE_p value and a higher I_p value compared to GCE. This result once again confirms the excellent electrical conductivity and electrocatalytic ability of bimetallic MOFs compared to monometallic MOFs. In the case of the GO/FeMg-BDC electrode, due to defects in the GO structure, the GO/FeMg-BDC electrode displays the lowest I_p values. By contrast, the rGO/FeMg-BDC electrode has the highest I_p and lowest ΔE_p values among all fabricated electrodes. This result is consistent with the EIS and further demonstrates that FeMg-BDC and rGO have created a synergistic effect that enhances the electron transfer rate on the electrode surface.

In addition, the Fe-BDC, FeMg-BDC, GO/FeMg-BDC, and rGO/FeMg-BDC electrodes underwent CV measurements in the
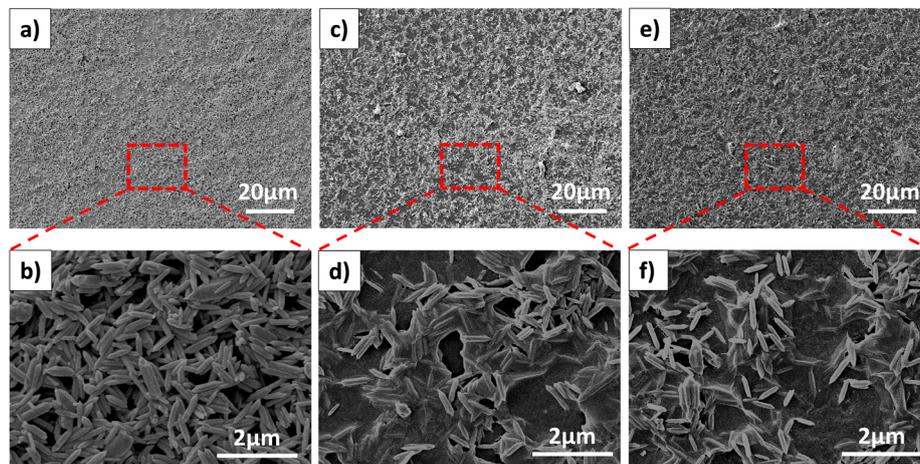

Fig. 3 The surface morphologies of FeMg-BDC (a and b), GO/FeMg-BDC (c and d), and rGO/FeMg-BDC (e and f) electrodes.
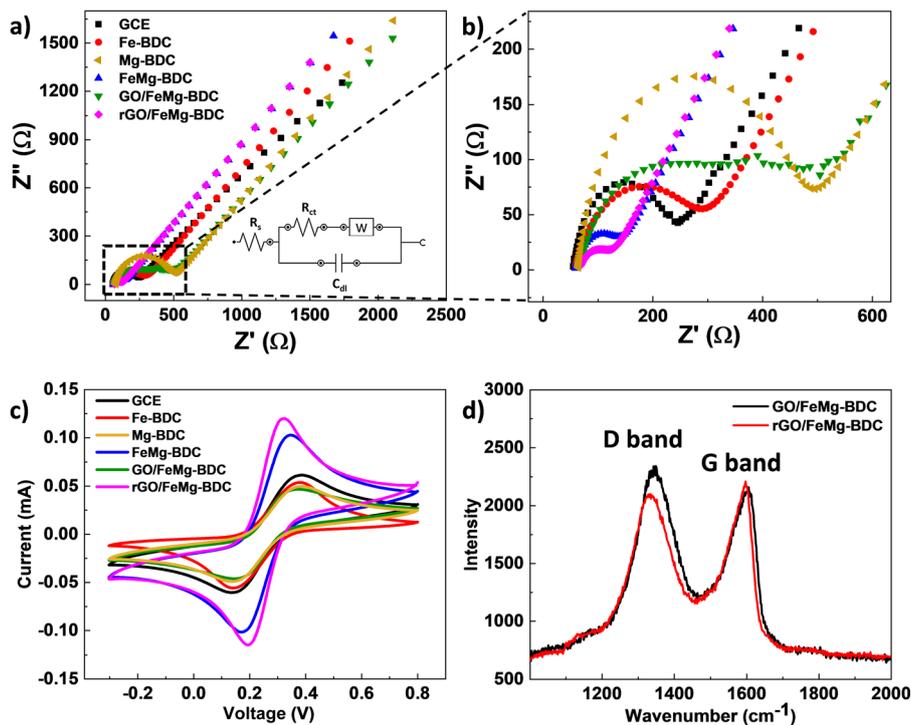
Fig. 4 (a and b) Nyquist plots and (c) CV redox current response at a scan rate of 0.05 V s^{-1} of the prepared electrodes in 0.1 M KCl solution containing 5 mM of [Fe(CN)$_6$]$^{3-/4-}$, (d) Raman spectrum of GO/FeMg-BDC and rGO/FeMg-BDC.

PBS solution at pH 7 (0.1 M) without K$_3$[Fe(CN)$_6$]. The results reveal no redox signal associated with iron, confirming that the iron content within the MOF does not influence the observed electrochemical signal (Fig. S3a†).

CV measurements were conducted at various scan rates to gain a better understanding of the electrochemical activity of the rGO/FeMg-BDC electrode (Fig. S3b†). The linear increase of peak current with the square root of the scan rate demonstrates the good electrochemical performance of the electrode (Fig. S3c†). Based on this result, the electrochemically active surface area is determined using Randles–Sevcik eqn (1).

$$I_{\mathrm{p}} = 2.69 \times 105 n^{3/2} A D^{1/2} C_{\mathrm{v}}^{1/2} \tag{1}$$

Here, the parameters are defined as follows: peak current (I_{p}), number of transferred electrons (n), electrochemically active surface area of the electrode (A), diffusion coefficient (D), concentration (C), and potential sweep rate (v). The obtained electrochemically active surface areas (EASA) of the GCE, Fe-BDC, Mg-BDC, FeMg-BDC, GO/FeMg-BDC, and rGO/FeMg-BDC were calculated to be 0.07, 0.055, 0.059, 0.12, 0.046 and 0.14 cm^2, respectively. According to these results, the rGO/FeMg-BDC electrode has the highest electrochemically active surface area value because the porous structure of FeMg-BDC and the rGO have a large surface area. The high electrochemically active surface area value is expected to facilitate the accumulation of Pb^{2+} onto the electrode surface thereby enhancing the performance of the sensor.

Raman spectroscopy was employed to characterize the GO/FeMg-BDC and rGO/FeMg-BDC layers on the electrodes,

elucidating the observed behavior and the effect of the electrochemical reduction process (Fig. 4d). The G band, a prominent feature observed in all sp^2 carbon systems, arises from C–C bond stretching vibrations. Conversely, the D band reflects the presence of structural defects and disorder within the graphene lattice. The present study observes the G band positions at 1606 cm^{-1} and 1594 cm^{-1} for GO/FeMg-BDC and rGO/FeMg-BDC, respectively. Additionally, the D band appears at 1348 cm^{-1} and 1336 cm^{-1}, respectively. Notably, the G band in rGO exhibits a slight down-shift compared to GO, potentially attributable to an increased abundance of sp^2 carbon atoms after electrochemical reduction. Furthermore, the decrease in the intensity ratio of the D band and the G band ($I_{\mathrm{D}}/I_{\mathrm{G}}$) from 1.1 (GO/FeMg-BDC) to 0.9 (rGO/FeMg-BDC) corroborates the successful removal of a significant portion of oxygen-containing functional groups and the formation of new sp^2 domains upon reduction.[34]

In comparison with the bare GCE as well as other modified electrodes, the rGO/FeMg-BDC electrode has the largest electrochemically active surface area and the highest charge transfer ability. Hence, rGO/FeMg-BDC is a promising candidate for the development of electrochemical sensors for lead ion detection.

3.3. Optimization of electrode preparation condition

3.3.1 Electrochemical signal of Pb^{2+} on different electrodes. The electrochemical signal of Pb^{2+} on the fabricated electrodes was recorded using the SWASV method. As shown in Fig. 5, an oxidation peak for Pb appears at about −0.43 V. The

proposed mechanism for the electrochemical detection of Pb^{2+} in aqueous solution is as follows: first, Pb^{2+} ions are adsorbed onto the MOF surface due to the electrostatic interaction between the positively charged Pb^{2+} ions and the negatively charged carboxylic groups of the MOF (Fig. S5†).[35] Next, the adsorbed Pb^{2+} ions are electrochemically reduced to metallic Pb on the electrode surface under an applied potential of −0.8 V. Finally, square-wave anodic stripping voltammetry (SWASV) is performed to oxidize Pb back to Pb^{2+}, producing the characteristic oxidation peak.[36] The mechanism is illustrated schematically in Fig. S6.†

The obtained results shown in Fig. 5 and Table 2 indicate that the GCE exhibits the lowest peak current. Although Fe-BDC and Mg-BDC have low charge transfer capacity, their electrochemical signals are higher than those of GCE due to the porous structure inside the MOF which enhances the adsorption of Pb^{2+} during the accumulation process. Owning a fast electron transfer rate, the FeMg-BDC electrode shows significantly higher oxidation peaks than that of the Fe-BDC and Mg-BDC electrodes.

The GO/FeMg-BDC electrode exhibits a high electrochemical signal although the charge transfer capability of the GO/FeMg-BDC electrode is low (Table 2). This phenomenon may be attributed to the partial reduction of GO to rGO during the accumulation step at −0.8 V. However, the competition between the reduction of GO and the deposition of Pb^{2+} might have hindered the complete reduction of GO. Consequently, the peak current value is lower than that of the rGO/FeMg-BDC electrode.
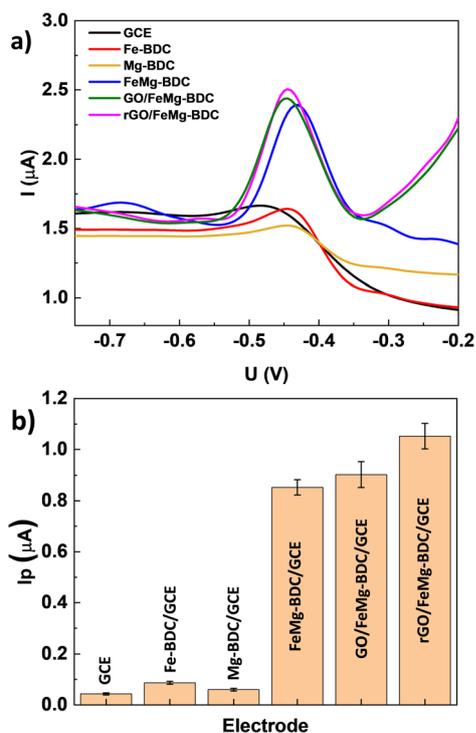
Table 2 Relationship between total electrode impedance, electrochemically active surface area, and peak current in Pb^{2+} analysis

Electrode	R_{ct} (Ω)	EASA (cm²)	I_p (μA)
GCE	180	0.07	0.05
Fe-BDC	229	0.055	0.11
Mg-BDC	398	0.059	0.07
FeMg-BDC	70	0.12	0.88
GO/FeMg-BDC	413	0.046	0.91
rGO/FeMg-BDC	55.7	0.14	1.08

Ultimately, the rGO/FeMg-BDC electrode exhibits the highest electrochemical signal, due to its excellent conductivity and extensive electrochemically active surface area.

The durability of FeMg-BDC and rGO/FeMg-BDC electrodes were also investigated (Fig. 6). The electrochemical signal of the FeMg-BDC electrode shows a significant decrease after each measurement. In contrast, the electrochemical signal of the rGO/FeMg-BDC electrode remains unchanged after 10 consecutive measurements with a relative standard deviation of 3.8%.

The electrode surface before and after Pb^{2+} analysis was studied using SEM images. After the first measurement, partly of the MOF material on the surface of the FeMg-BDC electrode is detached (Fig. 7). After the three measurements, there are only a few MOF crystals remained on the electrode surface. This phenomenon explains why the electrochemical signal decreased significantly. Meanwhile, for the rGO/FeMg-BDC
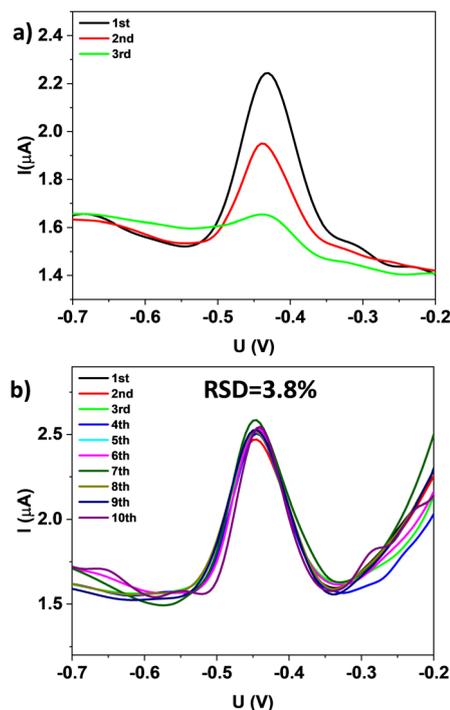

Fig. 5 (a) SWASVs of different electrodes and (b) the plot of peak current at different electrodes in 0.1 M KCl–HCl solution at pH 3 containing 1 μg per L Pb^{2+} and accumulation time of 120 s.

Fig. 6 SWASVs of (a) FeMg-BDC electrode and (b) rGO/FeMg-BDC electrode after several Pb^{2+} analysis measurements. All of these experiments were performed in 0.1 M of KCl buffer solution pH = 3 containing 1 μg per L Pb^{2+} with accumulation potential at −0.8 V during 120 s.
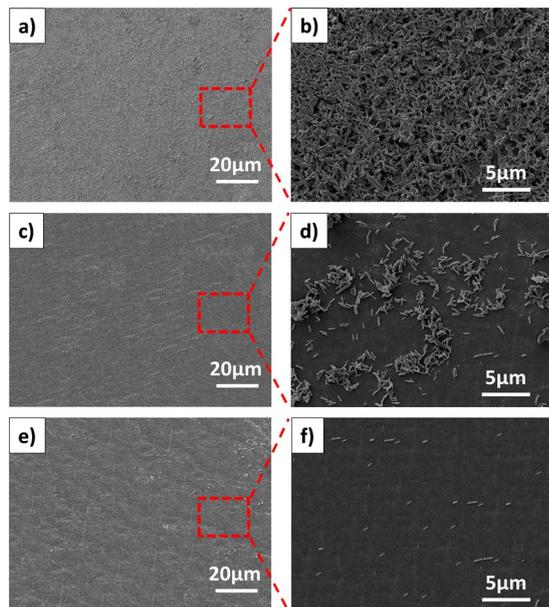
Fig. 7 SEM images of FeMg-BDC electrode surface (a and b) before and (c and d) after the first measurement, (e and f) after the third measurement.

electrode, the electrode surface remains durable after 10 measurements (Fig. 8), which is consistent with the obtained electrochemical signal. This result shows the effectiveness of the rGO layer on the electrode surface. When combined with bimetallic MOF, rGO acts as a thin protective film, shielding the underlying material layer from external influences during the analysis process. Based on the obtained results, it can be concluded that rGO/FeMg-BDC is a suitable electrode for lead ions electrochemical detection that requires high repeatability.

3.3.2 Influence of Fe/Mg ratio in bimetallic MOF on Pb^{2+} detection. The SWASV was recorded for rGO/FeMg-BDC electrodes with different ratios of Fe/Mg (Fig. 9a). The electrochemical signal indicates that the electrode employing a bimetallic MOF with a Fe/Mg ratio of 1/2 exhibits the highest electrochemical signal, followed by ratios of 1/1 and 1/4. This
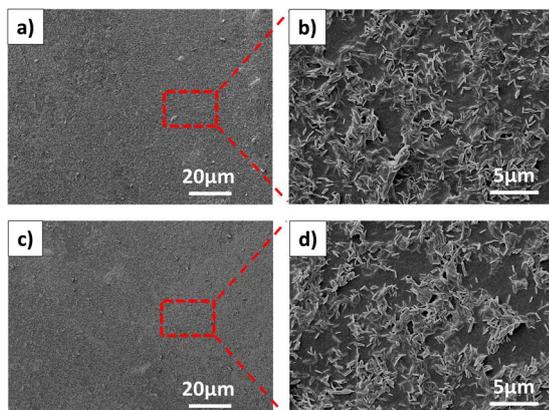

Fig. 8 SEM images of rGO/FeMg-BDC electrode surface (a and b) before and (c and d) after the 10 times of measurement.

observation is consistent with the surface area characteristics of the electrode materials (Table 1), revealing a direct relationship between surface area, pore volume, pore size, and the electrochemical performance of the electrodes. Specifically, the Fe–Mg MOF (1/2), which has the highest surface area, pore volume, and pore size, demonstrates a superior Pb^{2+} ion adsorption capacity. This leads to a significant enhancement of the electrochemical signal. Adsorption studies further reveal that Fe–Mg MOF (1/2) achieves an impressive Pb^{2+} adsorption efficiency of 91% within an adsorption time of 60 minutes, markedly higher than Fe–Mg MOF (1/1), Fe–Mg MOF (1/4), and the monometallic MOFs (Fig. S7†). This finding aligns with previous research that demonstrated the Fe/Mg ratio of 0.6 : 1 (approximately 1/2) to be the most effective for Pb^{2+} adsorption. This enhancement is attributed to the synergistic effect of the two metals, which could create new active sites within the bimetallic MOF structure, beneficial for Pb^{2+} adsorption.[26] Therefore, FeMg-BDC with a Fe/Mg ratio of 1/2 is the optimal choice for fabricating electrodes.

3.3.3 Influence of concentration of FeMg-BDC (1/2) on Pb^{2+} detection. The effect of FeMg-BDC concentrations on the Pb^{2+} analysis capability of the rGO/FeMg-BDC electrode was investigated (Fig. 9b). The Pb oxidation signal on the rGO/FeMg-BDC electrode rises when MOF concentration is increased from 0.25 to 0.5 mg mL^{-1}. This behavior may be due to the fact that when the MOF concentration is 0.25 mg mL^{-1}, the coating layer is too thin, resulting in a lack of active sites and poor electrochemical reaction. Therefore, increasing the MOF concentration could improve the Pb^{2+} enrichment on the electrode surface. However, when the MOF concentration exceeds 0.5 mg mL^{-1}, the overly thick MOF layer hinders charge transfer on the electrode surface, which leads to a decrease in the analytical signal.[37] Therefore, the optimal MOF concentration of 0.5 mg mL^{-1} represents a balance between providing sufficient active sites for Pb^{2+} adsorption and maintaining efficient charge transfer.

3.3.4 Influence of concentration of GO on Pb^{2+} detection. The effect of GO concentrations on the Pb^{2+} detection of the rGO/FeMg-BDC electrode was also investigated. The electrodes were fabricated using different GO concentrations (0.01%, 0.02%, 0.03%, and 0.04% w/w). Fig. 9c indicates that the current reaches the maximum at a GO concentration of 0.02% and decreases at higher concentrations. At low GO concentrations (0.01% and 0.02%), the electrochemical reduction process facilitates the formation of rGO, which significantly enhances electron transfer on the electrode surface. This improved electron transferability leads to an increase in the peak current. However, at higher GO concentrations (0.03% and 0.04%), the formation of a thicker rGO layer may block some of the effective active sites on FeMg-BDC, resulting in a reduction in the peak current of Pb. This result is in agreement with a previous study, which reported that excessive rGO content can limit the availability of active sites on MOF-based electrodes, thereby reducing the electrochemical response of Cu^{2+} and Pb^{2+}.[38]

In addition, the stability of rGO/FeMg-BDC electrodes across varying GO concentrations was assessed. Fig. 9d shows that all electrodes exhibit highly stability, maintaining consistent
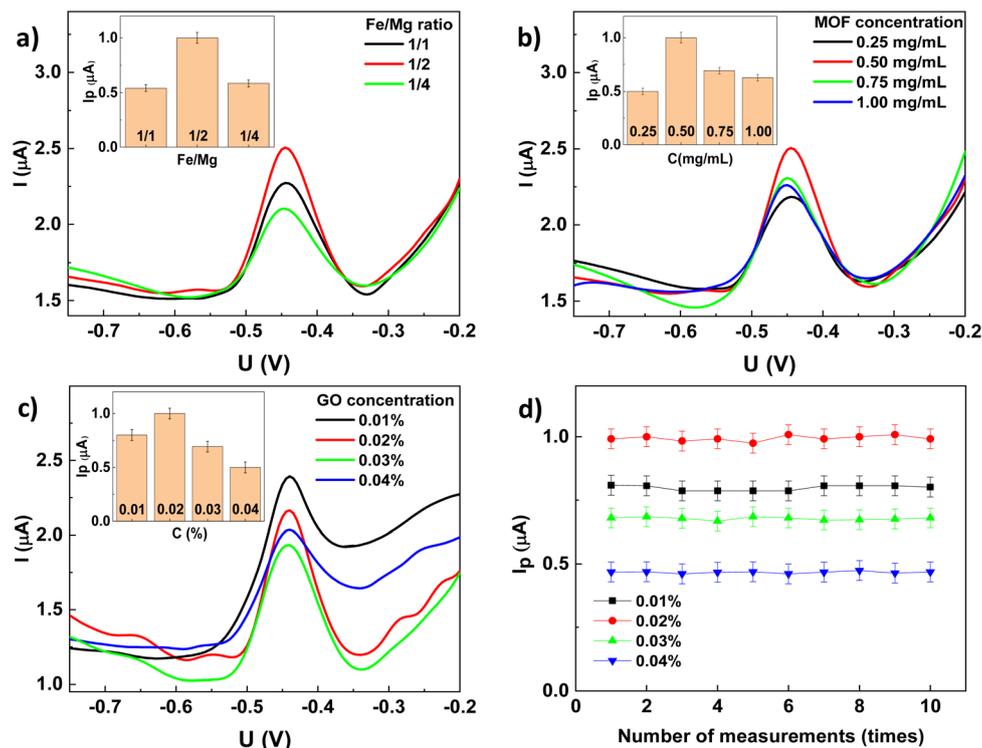
Fig. 9 SWASVs and (inset) plot of the peak current of rGO/FeMg-BDC electrode with (a) different ratios of Fe/Mg, (b) different concentrations of FeMg-BDC, (c) different concentrations of GO, (d) the plot of the peak current of rGO/FeMg-BDC electrode using different GO concentration after 10th measurement. All of these experiments were performed in 0.1 M of KCl–HCl solution pH = 3 containing 1 μg per L Pb^{2+} with accumulation potential at −0.8 V during 120 s.

electrochemical responses after 10 consecutive measurements. Then, GO solution with a concentration of 0.02% was selected to fabricate electrodes for further electrochemical analyses.

3.4. Optimization of analysis conditions

3.4.1 Supporting electrolyte. The impact of various electrolyte solutions, including sodium nitrate–nitric acid solution (NaNO$_3$–HNO$_3$), potassium chloride-hydrochloric acid solution (KCl–HCl), phosphate buffer solution (PBS), and acetate buffer solution (ABS) on the signal response of Pb^{2+} was systematically investigated at pH = 3. In the case of sodium nitrate, acetate, and phosphate buffers, the Pb^{2+} signals appear indistinct. Conversely, the KCl–HCl solution demonstrates a clear and well-defined Pb oxidation peak at about −0.45 V (Fig. 10a). This characteristic suggests that the KCL–HCl solution creates a favorable electrochemical environment leading to the efficient electrooxidation of Pb on the fabricated electrode. Therefore, the KCl–HCl solution was the optimal choice for enhancing the sensitivity of Pb^{2+} electrochemical analyses. The impact of various electrolyte solutions, including sodium nitrate–nitric acid solution (NaNO$_3$–HNO$_3$), potassium chloride-hydrochloric acid solution (KCl–HCl), phosphate buffer solution (PBS), and acetate buffer solution (ABS) on the signal response of Pb^{2+} was systematically investigated at pH = 3. In the case of sodium nitrate, acetate, and phosphate buffers, the Pb^{2+} signals appear indistinct. Conversely, the KCl–HCl solution demonstrates a clear and well-defined Pb oxidation peak at about −0.45 V

(Fig. 10a). This characteristic suggests that the KCL–HCl solution creates a favorable electrochemical environment leading to the efficient electrooxidation of Pb on the fabricated electrode. Therefore, the KCl–HCl solution was the optimal choice for enhancing the sensitivity of Pb^{2+} electrochemical analyses.

3.4.2 pH of supporting electrolyte. The influence of pH on the electrochemical signal was investigated within the range of 2.5–4, as depicted in Fig. 10b. The result in Fig. 10b shows that the highest peak was observed at pH 3.0. At elevated pH values, the peak height of the Pb oxidation signal notably diminished, accompanied by a shift toward more positive oxidation potentials. This observation indicates the favorable conditions for electrochemical Pb oxidation at lower pH values. Simultaneously, at higher pH levels, complexation occurs between Pb^{2+} ions and hydroxyl groups in the solution. Consequently, the enrichment capacity of Pb^{2+} ions on the electrode surface decreases. However, when pH = 2.5, the protonation degree of functional groups on the rGO surface is strong,[39] which is not conducive to the deposition of Pb^{2+} in the solution to the electrode surface. Therefore, pH 3.0 is optimal for electrochemical analysis in this study.

3.4.3 Deposition potential. In the Pb^{2+} analysis, an important factor is the deposition potential. The study examined the influence of the accumulation deposition process in the range from −0.7 to −1 V (Fig. 10c). The results show that when the potential increases from −0.7 to −0.8 V, the electrochemical signal increases and reaches a maximum value at −0.8 V. This
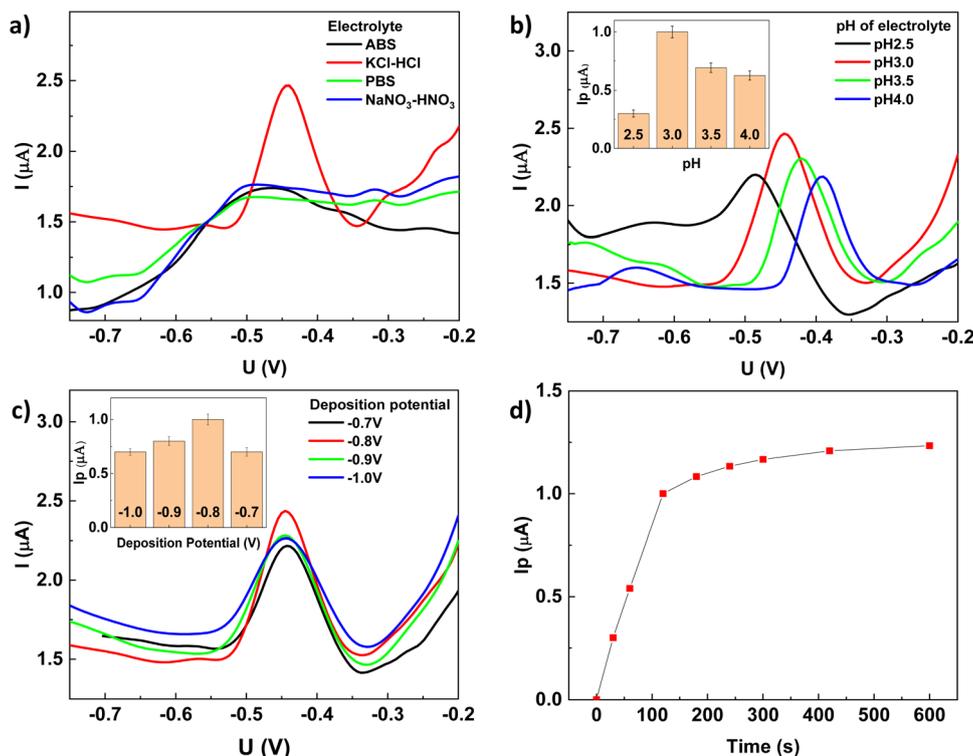
Paper

Fig. 10 SWASVs, and (inset) plot of the peak current of rGO/FeMg-BDC electrode (a) in different buffer solutions, (b) at different pH values, (c) at different accumulation potentials, (d) correlation between accumulation time and plot of the peak current of Pb^{2+} on rGO/FeMg-BDC electrode.

happens because, at a potential of -0.8 V, the supplied energy is sufficient to completely drive the electrochemical reduction of Pb^{2+} to Pb. However, at -0.9 V, the reduction of H^+ to hydrogen competes with the Pb^{2+} reduction process, leading to a decrease in the electrochemical signal. At -1 V, the hydrogen evolution becomes more pronounced, not only affecting the reduction of Pb^{2+} but also damaging the electrode surface, resulting in a significant decrease in the peak current of Pb. A similar observation has been reported in previous studies.[36,40,41] Based on these results, an accumulation potential of -0.8 V was selected for further analysis.

3.4.4 Accumulation time. The influence of accumulation time (t_{acc}) on the sensor response was explored by varying tacc from 0 to 600 seconds in 0.1 M KCl–HCl solutions (pH = 3) containing 1 μg per L Pb^{2+} (Fig. 10d). The peak current displays a significant increase as t_{acc} rose from 0 to 120 seconds, indicating enhanced Pb accumulation on the electrode surface.

However, from 120 seconds to 600 seconds, the peak height increases negligibly. The slow increase in peak height at longer adsorption times is attributed to the electrode surface nearing the equilibrium state of Pb^{2+} adsorption. The studied accumulation time is consistent with a previous study.[42] Consequently, the t_{acc} of 120 seconds is chosen to optimize sensitivity, reduce analysis time, and avoid saturation of the electrode surface.

3.5. Calibration curve for Pb^{2+} detection

The calibration curves for the Pb^{2+} detection with varying concentrations of Pb^{2+} (ranging from 0.01 to 50 μg L^{-1}) solution was constructed by recording SWASV in 0.1 M KCl–HCl at pH = 3 with deposition potential at -0.8 V during 120 s (Fig. 11a). Accordingly, the peak signal shows a good linear relationship with the Pb^{2+} concentration across two linear ranges with different slopes. The calibration curves for the two concentration ranges, from 0.01 μg L^{-1} to 0.5 μg L^{-1} and from 0.5 μg L^{-1} to 50 μg L^{-1}, are shown at higher magnification in Fig. 11b and d, with the regression equations being I_p (μA) = 1.7127 (μg L^{-1}) + 0.0148 and I_p (μA) = 0.16574 (μg L^{-1}) + 0.8334, respectively.

This result is attributed to the fact that, at low Pb^{2+} concentrations (from 0.01 μg L^{-1} to 0.5 μg L^{-1}), the accumulation process occurs rapidly both within the pores and on the outer surface of the material, which possesses a large specific surface area. This facilitates efficient enrichment of Pb^{2+}, leading to a sharp increase in the peak signal as the concentration rises. When the Pb^{2+} concentration exceeds 0.5 μg L^{-1}, the active sites on both the inner pores and the outer surface of the electrode material gradually become saturated. At that point, mass transport becomes limited, particularly within the porous structure. Consequently, the linear relationship between Pb^{2+} concentration and the analytical signal transitions to a second range with a reduced slope, forming a secondary calibration range. Additionally, the accumulation of Pb^{2+} at higher concentrations may occur in the form of multilayers, which could also contribute to the reduction in the slope of the linear calibration curve. This result aligns with several previously published studies, which have reported similar behaviors.[42,43] The SWASVs recorded at different concentrations on the rGO/FeMg-BDC electrode are presented in the Fig. 11c and d.
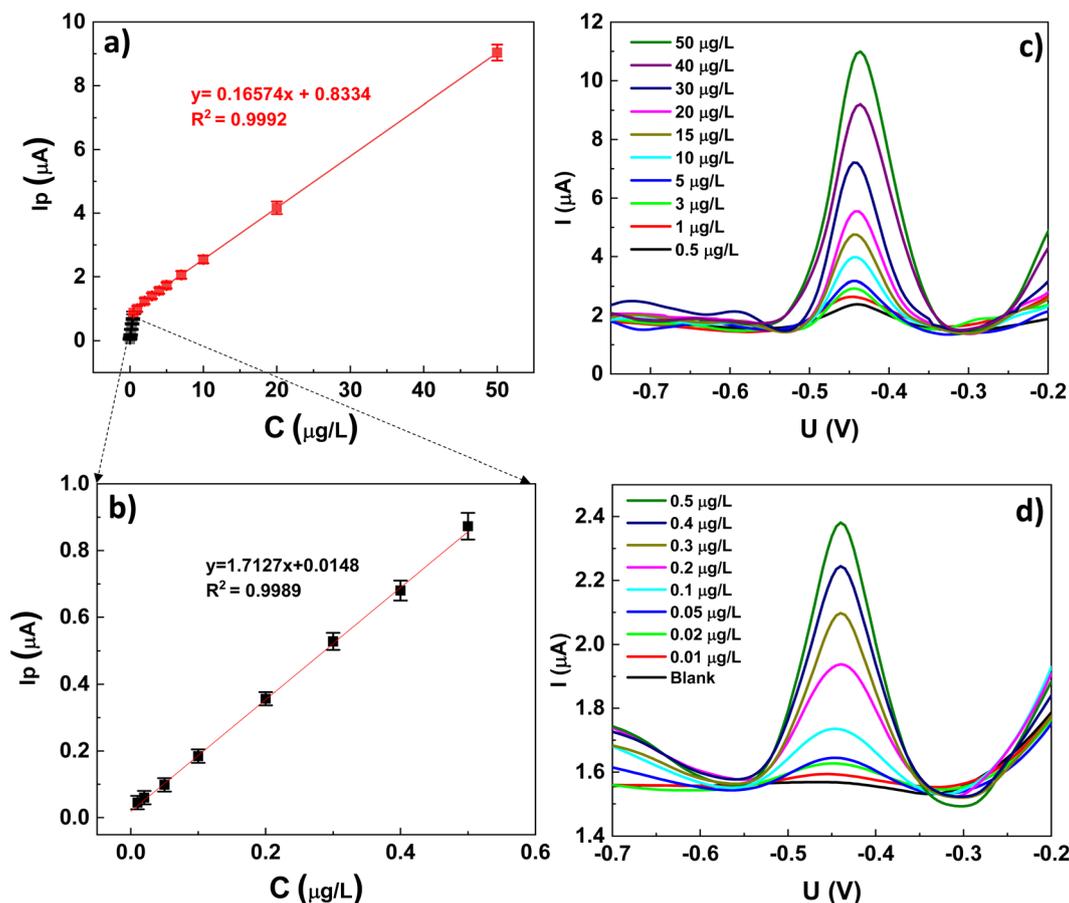
Fig. 11 Standard curve of peak current *versus* Pb^{2+} concentration (0.01–50 µg L^{-1}) (a); linear plots for Pb^{2+} concentrations from 0.01 to 0.5 µg L^{-1} (b). SWASVs of the rGO/FeMg-BDC electrode at various Pb^{2+} concentrations in a 0.1 M KCl–HCl solution (pH = 3), with an accumulation potential of −0.8 V for 120 s (c and d).

The limit of detection (LOD) represents the sensitivity of the analysis and is therefore calculated based on the most sensitive linear range of 0.01–0.5 µg per L Pb^{2+} using the standard deviation (σ) of the response from this calibration curve and its slope (Fig. 11b). The calculated LOD value was 0.009 µg L^{-1}, significantly lower than the permissible limit of 10 µg L^{-1} set by the World Health Organization (WHO) for lead in drinking water. The sensor performance was further evaluated by comparing its LOD with previously reported Pb^{2+} detection

sensors, as summarized in Table 3. The results indicated that the LOD value of this sensor was lower than many reported results.[19,20,44–50]

3.6. Reproducibility and durability over time of the rGO/FeMg-BDC electrode

To assess the reproducibility of the electrochemical sensor, the Pb^{2+} signals were measured across ten distinct rGO/FeMg-BDC electrodes under identical conditions. These results exhibit

Table 3 Performance of different electrochemical sensors for the determination of Pb^{2+}

Electrode	Method	Linear range (µg L^{-1})	LOD (µg L^{-1})	Ref.
Au@SiO$_2$@FMg–BDCO$_4$/NG/GCE	SWASV	5–80	0.60	44
GO–AgNW/PET	SWASV	0.2–60	0.067	45
NH$_2$-MIL-53(Al)/Ppy/BCE	DPV	1–400	0.31	46
NH$_2$-MIL-53(Cr)/GCE	SWASV	0.4–80	6.22	47
Zn$_4$O(BDC)$_3$/CPE	DPV	2.07–207	1	48
NH$_2$-MIL-101(Fe)/CPE	DPV	20.7–2070	2.48	49
NH$_2$-MIL-88(Fe)–rGO/GCE	DPV	2.07–62	2.07	20
GA-UiO-66-NH$_2$/GCE	DPV	2.07–828	0.3	19
MOF-808-His/GCE	SWASV	0.207–103	0.023	50
rGO/Fe–Mg-BDC/GCE	SWASV	0.01–50	0.009	This work

Paper

insignificant differences between electrochemical signals (Fig. S5a†), and the relative standard deviation (RSD) for the ten measurements is 3.1% (Fig. S5b†). The obtained result indicates that the fabricated sensor had good reproducibility.

The durability over time of the rGO/FeMg-BDC electrode was evaluated using the SWASV method analyzing Pb^{2+} every 5 days for 30 days. The electrode was stored between measurements under ambient conditions. The electrode shows stable SWASV signals during the 30 days measurement (Fig. S6a and b†). This observation indicates high temporal stability for the rGO/FeMg-BDC electrode.

3.7. Selectivity of the rGO/FeMg-BDC electrode

The selectivity of the electrochemical sensor based on the rGO/FeMg-BDC electrode was examined under optimal conditions in the presence of various inorganic and organic substances. Fig. S7† illustrates the change of signal peak height by adding 100 μg L^{-1} of inorganic ions or organic compounds to a 1 μg L^{-1} solution of Pb^{2+} (100-fold). Except PO_4^{3-}, all inorganic ions cause minimal interference to the Pb^{2+} signal, showing relative errors below 5%. The effect of PO_4^{3-} on the electrochemical signal could be explained by the formation of complexes between PO_4^{3-} and Pb^{2+} in solution. Furthermore, the presence of organic substances including paracetamol, uric acid, glucose, ascorbic acid, and dopamine at concentrations 100 times higher than that of Pb^{2+} do not significantly affect the Pb^{2+} electrochemical signal recorded on the rGO/FeMg-BDC electrode. Thus, the analysis method employing the fabricated sensor exhibits high selectivity in solutions containing high inorganic and organic substance concentrations.

3.8. Determination of Pb^{2+} in real samples

Ha Long Bay seawater (Ha Long, Quang Ninh, Viet Nam, with specific coordinates 20°56′44.3″N, 107°02′38.7″E), West Lake water (Tay Ho, Hanoi, Viet Nam, with specific coordinates 21°04′08.1″N, 105°48′45.1″E), and Red River water (Tay Ho, Hanoi, Vietnam, with specific coordinates 21°05′27.0″N, 105°48′43.4″E) were used to evaluate the performance of the sensor in the determination of Pb^{2+} in real samples. Water samples were collected on-site in polyethylene bottles and nitric acid was added to stabilize the sample. To avoid sample dilution, KCl was added to the water samples as an electrolyte ([KCl] = 0.1 M). After that, the samples were used as a normal KCl buffer solution.

The applicability of the fabricated electrode for Pb^{2+} detection in real samples was assessed using the standard addition method. The relative standard deviation (RSD) was determined by measuring each sample three times. Pb^{2+} concentrations have values of 3.29 μg L^{-1}, 0.20 μg L^{-1}, and 2.65 μg L^{-1} for Ha Long seawater, Red River water, and West Lake water samples, respectively (Table 4 and Fig. S8†). These results are similar to those obtained via inductively coupled plasma mass spectrometry (ICP-MS), demonstrating good accuracy of the rGO/Fe–Mg-BDC/GCE sensor for Pb^{2+} detection in real samples.

4. Conclusion

In this study, an innovative electrochemical sensor was developed by modifying a glassy carbon electrode with a unique combination of FeMg-BDC and reduced graphene oxide (rGO) for the sensitive and selective detection of Pb^{2+} ions. The bimetallic architecture of FeMg-BDC enhances charge transfer efficiency and specific surface area, while the integration of rGO further improves the sensor's electrochemical properties and significantly boosts its durability. This synergy results in exceptional analytical performance, including a low detection limit, wide linear dynamic range, good selectivity, high reproducibility, and long-term stability. The practical utility of the sensor was validated by accurately quantifying lead ion concentrations in sea, river, and lake water samples, highlighting the potential of the rGO/FeMg-BDC/GCE electrode for reliable lead ion detection in analytical applications.

Data availability

The data supporting this article have been included as part of the ESI.†

Author contributions

Conceptualization, Mai Ha Hoang, Thi Hai Yen Pham; data analysis, Tien Dat Doan, Thu Thao Le, Nhung Hac Thi; methodology, Tien Dat Doan, Dinh Dung Luong, Ho Thi Oanh; project administration, Mai Ha Hoang, Thi Kim Dung Hoang; validation, Ha Tran Nguyen; writing – original draft, Tien Dat Doan, Thi Hai Yen Pham; writing – review & editing, Mai Ha Hoang and Thi Hai Yen Pham. All authors have read and agreed to the published version of the manuscript.

Conflicts of interest

There are no conflicts of interest to declare.

Acknowledgements

References

1 A. Alengebawy, S. T. Abdelkhalek, S. R. Qureshi and M. Q. Wang, *Toxics*, 2021, **9**, 40–48.

Table 4 Analytical results for the determination of Pb^{2+} in different water samples

Sample	Determined by electrochemical sensor		Determined by ICP-MS (μg L^{-1})
	Conc. (μg L^{-1})	RSD (%)	
Ha long seawater	3.29	3.4	3.34
Red river water	0.2	4.6	0.21
West lake water	2.65	3.5	2.69

2 A. Waheed, M. Mansha and N. Ullah, *TrAC, Trends Anal. Chem.*, 2018, **105**, 37–51.

3 P. J. Mafa, A. O. Idris, N. Mabuba and O. A. Arotiba, *Talanta*, 2016, **153**, 99–106.

4 D. Anh Nguyen, D. Viet Nguyen, G. Jeong, N. Asghar and A. Jang, *J. Chem. Eng.*, 2023, **461**, 141789.

5 H. Xing, J. Xu, X. Zhu, X. Duan, L. Lu, Y. Zuo, Y. Zhang and W. Wang, *J. Electroanal. Chem.*, 2016, **782**, 250–255.

6 H. Ebrahimzadeh and M. Behbahani, *Arab. J. Chem.*, 2017, **10**, S2499–S2508.

7 S. V. Smirnova, T. O. Samarina, D. V. Ilin and I. V. Pletnev, *Anal. Chem.*, 2018, **90**, 6323–6331.

8 T. T. Shih, C. C. Hsieh, Y. T. Luo, Y. A. Su, P. H. Chen, Y. C. Chuang and Y. C. Sun, *Anal. Chim. Acta*, 2016, **916**, 24–32.

9 A. C. Sotolongo, M. M. Messina, F. J. Ibanez and R. G. Wuilloud, *Talanta*, 2020, **210**, 120614.

10 T. D. Doan, Y. T. H. Pham, H. T. Nhung, H. T. Oanh, T. N. Duc, H. Q. Le, T. H. T. Vu, P. H. Pham and M. H. Hoang, *Vietnam J. Chem.*, 2024, 70–79.

11 P. Wu, S. Li, X. Ye, B. Ning, J. Bai, Y. Peng, L. Li, T. Han, H. Zhou, Z. Gao and P. Ding, *Anal. Chim. Acta*, 2020, **1134**, 96–105.

12 C. Canales, E. Peralta and M. Antilen, *J. Electroanal. Chem.*, 2019, **832**, 329–335.

13 C. Gao and X.-J. Huang, *TrAC, Trends Anal. Chem.*, 2013, **51**, 1–12.

14 D. A. Nguyen, D. V. Nguyen, G. Jeong, N. Asghar and A. Jang, *J. Hazard. Mater.*, 2023, **460**, 132126.

15 N. Asghar, A. Hussain, D. A. Nguyen, S. Ali, I. Hussain, A. Junejo and A. Ali, *J. Nanobiotechnol.*, 2024, **22**, 26.

16 Q. L. Zhu and Q. Xu, *Chem. Soc. Rev.*, 2014, **43**, 5468–5512.

17 S. Tajik, H. Beitollahi, F. Garkani Nejad, I. Sheikhshoaie, A. S. Nugraha, H. W. Jang, Y. Yamauchi and M. Shokouhimehr, *J. Mater. Chem. A*, 2021, **9**, 8195–8220.

18 N. Kajal, V. Singh, R. Gupta and S. Gautam, *Environ. Res.*, 2022, **204**, 112320.

19 M. Lu, Y. Deng, Y. Luo, J. Lv, T. Li, J. Xu, S. W. Chen and J. Wang, *Anal. Chem.*, 2019, **91**, 888–895.

20 S. Duan and Y. Huang, *J. Electroanal. Chem.*, 2017, **807**, 253–260.

21 Z. Xu, Q. Wang, H. Zhangsun, S. Zhao, Y. Zhao and L. Wang, *Food Chem.*, 2021, **349**, 129202.

22 L. S. Xie, G. Skorupskii and M. Dinca, *Chem. Rev.*, 2020, **120**, 8536–8580.

23 L. Sun, M. G. Campbell and M. Dinca, *Angew. Chem., Int. Ed. Engl.*, 2016, **55**, 3566–3579.

24 J. Wan, Y. Shen, L. Xu, R. Xu, J. Zhang, H. Sun, C. Zhang, C. Yin and X. Wang, *J. Electroanal. Chem.*, 2021, **895**, 115374.

25 J. H. Choi, Y. J. Choi, J. W. Lee, W. H. Shin and J. K. Kang, *Phys. Chem. Chem. Phys.*, 2009, **11**, 628–631.

26 W. S. Abo El-Yazeed, Y. G. Abou El-Reash, L. A. Elatwy and A. I. Ahmed, *RSC Adv.*, 2020, **10**, 9693–9703.

27 Y. Gu, D. Xie, Y. Wang, W. Qin, H. Zhang, G. Wang, Y. Zhang and H. Zhao, *J. Chem. Eng.*, 2019, **357**, 579–588.

28 D. Huo, Y. Zhang, N. Li, W. Ma, H. Liu, G. Xu, Z. Li, M. Yang and C. Hou, *Anal. Bioanal. Chem.*, 2022, **414**, 1575–1586.

29 A. M. Dimiev and J. M. Tour, *ACS Nano*, 2014, **8**, 3060–3068.

30 A. Viinikanoja, Z. Wang, J. Kauppila and C. Kvarnstrom, *Phys. Chem. Chem. Phys.*, 2012, **14**, 14003–14009.

31 X. Yao, C. Bai, J. Chen and Y. Li, *RSC Adv.*, 2016, **6**, 26921–26928.

32 D. Roy, S. Neogi and S. De, *J. Hazard. Mater.*, 2021, **403**, 123624.

33 F. Ahmadijokani, S. Tajahmadi, A. Bahi, H. Molavi, M. Rezakazemi, F. Ko, T. M. Aminabhavi and M. Arjmand, *Chemosphere*, 2021, **264**, 128466.

34 V. Scardaci and G. Compagnini, *C*, 2021, **7**, 48.

35 R. Soltani, R. Pelalak, M. Pishnamazi, A. Marjani, A. B. Albadarin, S. M. Sarkar and S. Shirazian, *Sci. Rep.*, 2021, **11**, 1609.

36 L. Yu, X. Chen, L. Sun, Q. Zhang, B. Yang, M. Huang, B. Xu and Q. Xu, *React. Funct. Polym.*, 2024, **194**, 105770.

37 C. Yao, H. Wang, J. Zhou, W. Song, Q. Rao, Z. Gao, C. Liu, W. Song and Y. Liang, *Arab. J. Chem.*, 2024, **17**, 105498.

38 Z. Li, X. Zhang, Y. Luo, Q. Li, Y. Qin, G. Wang, S. Yang and Z. Liu, *Chem. Phys. Lett.*, 2023, **830**, 140825.

39 H. Huang, J. Wang, Y. Zheng, W. Bai, Y. Ma and X. Zhao, *Food Chem.*, 2024, **452**, 139572.

40 L. D. Nguyen, T. C. D. Doan, T. M. Huynh, V. N. P. Nguyen, H. H. Dinh, D. M. T. Dang and C. M. Dang, *Sens. Actuators, B*, 2021, **345**, 130443.

41 F. Gholami, M. Roushani, H. Hosseini and Z. M. Karazan, *Microchem. J.*, 2024, **201**, 110634.

42 H. Liu, H. Sun, M. Fang, Y. Zhang, M. Kong, Z. Lv and X. Tan, *Mater. Chem. Phys.*, 2024, **314**, 128833.

43 Z. Lu, W. Zhao, L. Wu, J. He, W. Dai, C. Zhou, H. Du and J. Ye, *Sens. Actuators, B*, 2021, **326**, 128957.

44 J. Nie, B. He, Y. Cheng, W. Yin, C. Hou, D. Huo, L. Qian, Y. Qin and H. Fa, *Chem. Res. Chin. Univ.*, 2017, **33**, 951–957.

45 T. T. H. Nguyen, T. H. Y. Pham, T. D. Doan, N. H. Thi, H. T. Oanh, T. T. Nguyen, V. T. T. Ha, T. Van Nguyen, M. J. Cho, D. H. Choi and M. H. Hoang, *Chem. Pap.*, 2022, **76**, 5459–5469.

46 N. Wang, W. Zhao, Z. Shen, S. Sun, H. Dai, H. Ma and M. Lin, *Sens. Actuators, B*, 2020, **304**, 127286.

47 H. Guo, D. Wang, J. Chen, W. Weng, M. Huang and Z. Zheng, *J. Chem. Eng.*, 2016, **289**, 479–485.

48 Y. Wang, Y. Wu, J. Xie and X. Hu, *Sens. Actuators, B*, 2013, **177**, 1161–1166.

49 P. Chen, H. Wang, H. Li, B. Niu, H. Guo and Z. Chen, *J. Electroanal. Chem.*, 2024, **957**, 118–129.

50 S. L. Z. Jiokeng, T. J. Matemb Ma Ntep, M. N. A. Fetzer, T. Strothmann, C. G. Fotsop, I. Kenfack Tonle and C. Janiak, *ACS Appl. Mater. Interfaces*, 2024, **16**, 2509–2521.